

An Azo-Bridged Ferroelectric Liquid Crystal with Highly Enhanced Second and Third Harmonic Generation

Yongqiang Zhang,^{*,†} Josu Ortega,[‡] Ute Baumeister,^{||} César L. Folcia,[§] Gerardo Sanz-Enguita,[‡] Christopher Walker,[†] Sofía Rodríguez-Conde,[§] Jesus Etxebarria,^{*,§} Michael J. O'Callaghan,[†] and Kundalika More[†]

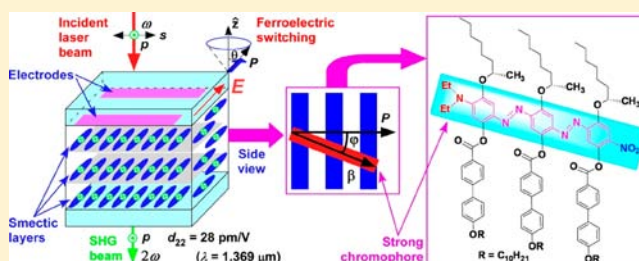
[†]Micron Technology Inc., 2602 Clover Basin Drive, Longmont, Colorado 80503, United States

[‡]Department of Applied Physics II, [§]Condensed Matter Physics, University of the Basque Country, UPV/EHU, 48080 Bilbao, Spain

^{||}Institute of Chemistry, Physical Chemistry, MLU Halle-Wittenberg, Kurt-Mothes-Strasse 2, D-06120 Halle, Germany

Supporting Information

ABSTRACT: A laterally azo-bridged trimer ferroelectric liquid crystal (FLC) incorporating a strong chromophore along its polar axis was synthesized and characterized by polarized-light optical microscopy, differential scanning calorimetry, two-dimensional X-ray diffraction analysis, electro-optical measurements, and nonlinear optical (NLO) investigations. This mesogen exhibits a thermodynamically stable enantiotropic SmC* phase and a bistable ferroelectric switching in a surface stabilized cell with bookshelf geometry. It gives the resonance-enhanced d_{22} coefficient of 28 pm V^{-1} ($\lambda = 1.369 \mu\text{m}$) for second harmonic generation (SHG), the largest NLO susceptibility reported to date for all FLCs. At the same wavelength, a new type of helicoidal phase matching assisted by the helical SmC* structure was identified. When the second harmonic wavelength of 780 nm is far away from the resonance wavelength ($\lambda_{\text{max}} = 572 \text{ nm}$), the d_{22} coefficient is reduced to 6.8 pm V^{-1} ($\lambda = 1.56 \mu\text{m}$). In addition to a strong SHG activity, the trimer also shows a strong third harmonic generation (THG) with an estimated third-order nonlinear susceptibility of $\chi^{(3)} = \sim 3 \times 10^{-11} \text{ esu}$ ($\lambda = 1.56 \mu\text{m}$), among the largest $\chi^{(3)}$ value reported from THG measurements for liquid crystals. This work enables viable applications of FLCs in nonlinear optics and offers an innovative approach to develop new FLCs with larger NLO strength.



INTRODUCTION

Nonlinear optical (NLO) effects, mainly represented by second- and third-order effects, allow for laser modulation and have found a wide range of applications in electro-optic, optoelectronic, photonic, and biomedical technologies as well. Today's bench-mark NLO materials are actually inorganic crystals (e.g., LiNbO₃), but organic NLO materials offer greater opportunities for developing potentially low-cost and high-performance electronic and photonic devices because of their attractive features, such as large and ultrafast responses, low drive voltages, facile fabrication and processability, and wide range of operating frequencies.^{1,2} Organic NLO materials are easily integrated with silicon, enabling chip-scale integration of electronics and photonics into a complex individual device.³

Ferroelectric liquid crystals (FLCs),⁴ as a special type of organic NLO material, will become a compelling alternative to inorganic crystals and/or electrically poled organic glasses (i.e., poled polymers) if large NLO strength is achieved.^{5,6} Since FLCs possess thermodynamically stable polar order from self-assembled tilted smectic layer structures, they are inherently suitable for second harmonic generation (SHG). Hence both qualitative and quantitative SHG experiments have been widely applied to liquid crystal research and development.^{5,7,8} The

polar direction in an FLC can be electrically controlled by switching between two ferroelectric states, enabling fabrication of more complex NLO devices. Helicoidal structures in a FLC provide a special way for phase matching (PM) during an SHG process,⁹ and unwinding/winding such structures using an electric field (E-field) permits to obtain SHG switching.¹⁰ Orienting chromophores in FLCs requires a much weaker E-field than the poling technique in poled polymers (~ 1 vs $10\text{--}50 \text{ V } \mu\text{m}^{-1}$). Furthermore, as in successful liquid crystal displays, FLCs are compatible with well-established very large scale integration (VLSI) semiconductor electronic technology (e.g., Micron's FLCOS technology), offering a NLO material platform for hybrid technologies.

To enable viable NLO applications of an FLC, incorporating a strong chromophore with a large hyperpolarizability (β) along the FLC's polar axis is a prerequisite.⁵ Although numerous strong NLO chromophores have been developed for poled polymers,¹¹ realizing such a goal with liquid crystals is still very challenging because in most cases the required SmC* phase is killed upon incorporating a big chromophore into a rod-shaped

Received: June 27, 2012

Published: August 21, 2012

FLC along its polar axis. Consequently, the size of NLO coefficients for FLCs has been insufficient for decades.¹² We have recently reported that a dimer FLC 2, including a DR-1 chromophore (Figure 1) derived from Walba dimers,¹³

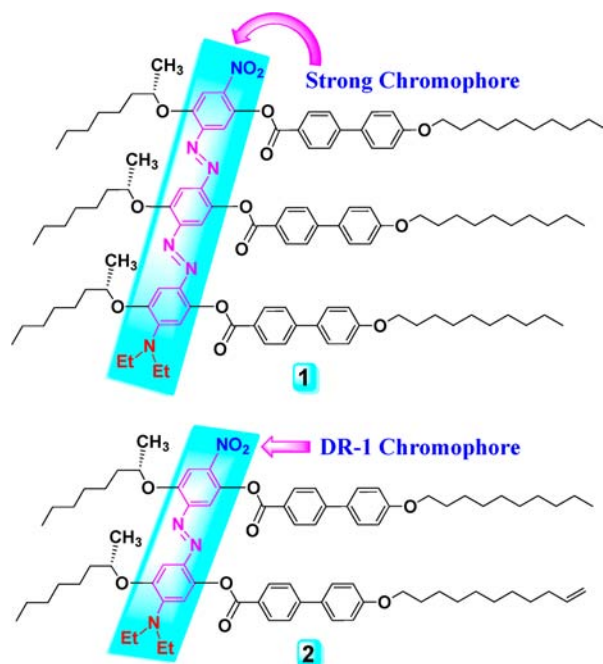


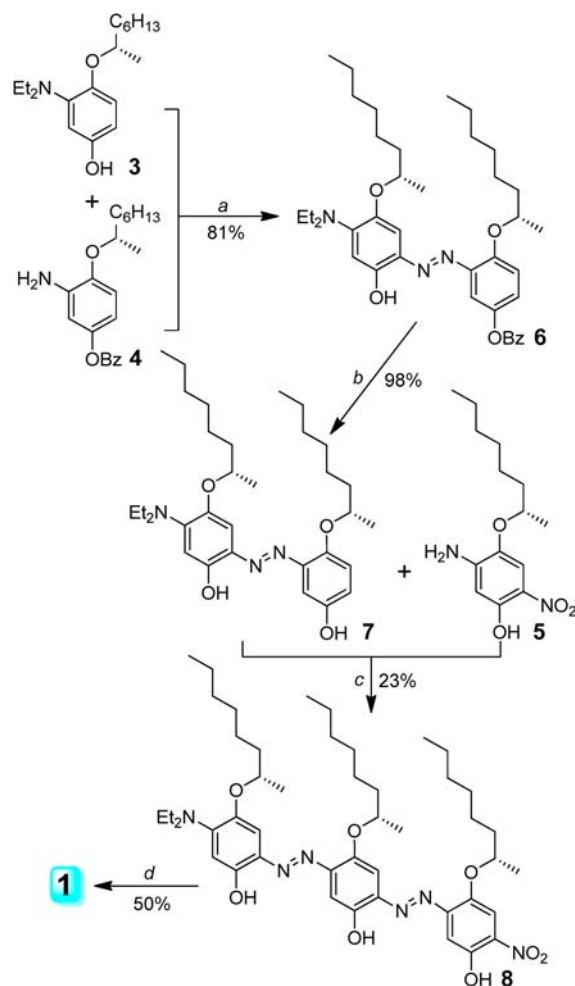
Figure 1. Structures of trimer **1** and dimer **2** with their chromophores highlighted.

exhibited the largest NLO coefficient of $d_{22} = 17 \text{ pm V}^{-1}$ ($\lambda = 1.064 \mu\text{m}$) for calamitic NLO FLCs.¹⁴ Herein we report that a trimer FLC **1** incorporating a stronger chromophore along its polar axis (Figure 1) gives a larger d_{22} coefficient of 28 pm V^{-1} ($\lambda = 1.369 \mu\text{m}$). To the best of our knowledge, this is the largest coefficient reported to date for all NLO FLCs. It is particularly noteworthy that compound **1** incorporating three rod-shaped units into such a big molecule exhibits a thermodynamically stable enantiotropic ferroelectric phase and rarely observed helicoidal phase matching (HPM) in the SHG process ($\lambda = 1.369 \mu\text{m}$). In addition to a strong SHG response, compound **1** also demonstrates a strong third harmonic generation (THG) response.

RESULTS AND DISCUSSION

Synthesis. The synthesis of compounds **1** is outlined in Scheme 1. Three precursors for diazo coupling reactions, **3–5**, were synthesized from 4-benzyloxyphenol by a literature approach^{13a} (for **4** and **5**) and a multistep approach¹⁴ (for **3**) involving reductive amination¹⁵ and hydrolysis under basic conditions. Subsequent diazo coupling,¹⁶ followed by the hydrolysis of the resultant ester under mild conditions, afforded the diphenol **7** in good overall yield. The second diazo coupling between the diphenol **7** and the *ortho*-nitro phenol **5** afforded the triphenol **8** in 23% yield after purification via flash chromatography. It is notable that the azo coupling occurs only at the position *ortho* to the hydroxy group of compound **7** rather than that *ortho* to both the hydroxy and diethylamino group presumably due to steric effect. This regioselectivity enables the synthesis of the target triphenol **8**. With the triphenol **8** in hand, esterification with an excess amount of 4'-

Scheme 1. Synthesis of Trimer **1** Incorporating a Strong Chromophore^a



^aReagents and conditions: (a) **4**, HCl, NaNO₂; then **3**, K₂CO₃, EtOH, CH₂Cl₂. (b) LiOH, THF, EtOH, H₂O. (c) **5**, HCl, NaNO₂, EtOH/H₂O; then **7**, pyridine, CH₂Cl₂, EtOH. (d) 4'-decyloxybiphenyl-4-carboxylic acid chloride, DMAP, Et₃N, THF.

decyloxybiphenyl-4-carboxylic acid chloride in the presence of dimethylaminopyridine (DMAP) and triethylamine (Et₃N) gave **1** in 50% yield. To obtain **1** in high purity, preparative thin-layer chromatography (TLC) was further employed to purify **1** after purification via flash chromatography. All new compounds were characterized by ¹H and ¹³C NMR and LC-MS (see detailed synthetic procedures and analytic data in Supporting Information). Compounds **1** and **8** were further characterized by elemental analysis. Analytic data are in good agreement with the proposed structures.

LC Phases of Mesogen **1 Incorporating a Strong Chromophore.** The liquid crystalline phases were characterized by polarized-light optical microscopy (POM), differential scanning calorimetry (DSC), X-ray diffraction (XRD) analysis, and electro-optical (EO) techniques. Phase transition temperatures and UV–vis spectroscopic data for compounds **1** and **2** are summarized in Table 1. Compound **1** exhibits an enantiotropic phase sequence of Cr-SmC*-N*-Iso. Like dimer **2**, trimer **1** shows suppression of crystallization, and its SmC* phase is also supercooled to the glassy state (gSmC*) around room temperature. However, **1** exhibits a much higher N*-SmC* phase transition temperature and broader SmC* phase

Table 1. Mesophases, Phase-Transition Temperatures, Maximum Absorption Wavelengths (λ_{\max}), and Corresponding Extinction Coefficients (ϵ_{\max}) of Compounds 1 and 2^a

compd	T , °C	λ_{\max} nm	ϵ_{\max} M ⁻¹ cm ⁻¹
1	Cr ₁ 84 Cr ₂ 123 SmC* 135 N* 146 Iso 145 N* 134 SmC* 31 gSmC*	572	27 700
2 ^b	Cr 73 SmC* 78 Iso 73 SmC* 14 gSmC*	531	33 912

^aPhase transition temperatures determined by DSC at 10 K min⁻¹ with two consecutive heating/cooling runs (top, heating; bottom, cooling) from -10 (or 200) to 200 (or -10) °C; and mesophases assigned by the analysis of DSC and 2D XRD data together with POM and EO investigations. Abbreviations: Iso = the isotropic liquid; gSmC* = the glassy state of the SmC* phase; and Cr = the crystalline state. The isotropic melt was stored in vials at room temperature for weeks prior to DSC measurements, and UV-vis spectra were taken in diluted CH₂Cl₂ solution. ^bData from ref 14. Note that phase transition temperatures are from the second heating run and the first cooling run, and the suppression of crystallization with cold crystallization at 68 °C was observed for 1 (Figure S1). The possible TGBA* phase observed by POM at 134 °C during cooling is not included in the phase sequence. The data for compound 2 are included for comparison.

temperature range (103 K) during cooling than 2, indicating that the incorporation of an additional rod into 2 greatly stabilizes the SmC* phase. In the second DSC heating run, compound 1 shows a cold crystallization at 68 °C preceding two probably (soft) crystal-crystal transitions prior to melting into the SmC* phase (Figure S1).

Upon cooling compound 1 from the isotropic liquid, a thread-like texture (Figure 2a) was initially formed, suggesting a cholesteric (N*) phase. Slowly cooling from the N* phase produced a typical filament texture (Figure S2) at 134 °C which is tentatively assigned as a twist grain boundary phase (TGBA*).¹⁷ The formation of small domains with very low birefringence in a homeotropic wedge cell and a droplet^{17b} prevented us from further investigating the TGBA* phase. Further cooling led to a fan-shaped focal conic texture (Figures 2c and S2), which supports the SmC* phase. The electrical polarization switching was observed in the SmC* phase upon the application of an alternating current (ac) E-field. The switching current curve (Figure 2e) shows a single current peak under an applied triangular wave (TW) E-field, indicating a ferroelectric (FE) switching. Square wave (SW) optical responses were obtained in all cases when different types of ac E-fields were employed (Figure 2f), and the transmission changes were frequency independent. These results strongly indicate a bistable FE switching rather than an analog V-shaped switching. The polarization reversal current peak was also observed under an applied SW E-field, and the integration of the peak area gave a measured spontaneous polarization of ~27 nC cm⁻² at 120 °C,¹⁸ which is smaller than those reported for NLO monomers^{12b} and dimers.^{13a,14} The spontaneous polarization was found to slightly increase with decreasing temperature through the SmC* phase, as is typical for conventional rod-shaped FLC materials with an N*-SmC* phase transition. Under an applied SW E-field (10 V μm^{-1}), the switching time constant of 1 was 1.2 ms at 120 °C, much slower than conventional rod-shaped FLCs (70–90 μs under 6 V μm^{-1} at room temperature), indicating high-rotational viscosity of molecules of 1.

Upon cooling a film sample of 1, crystallization generally occurred when the cell was kept around 60–80 °C for a long

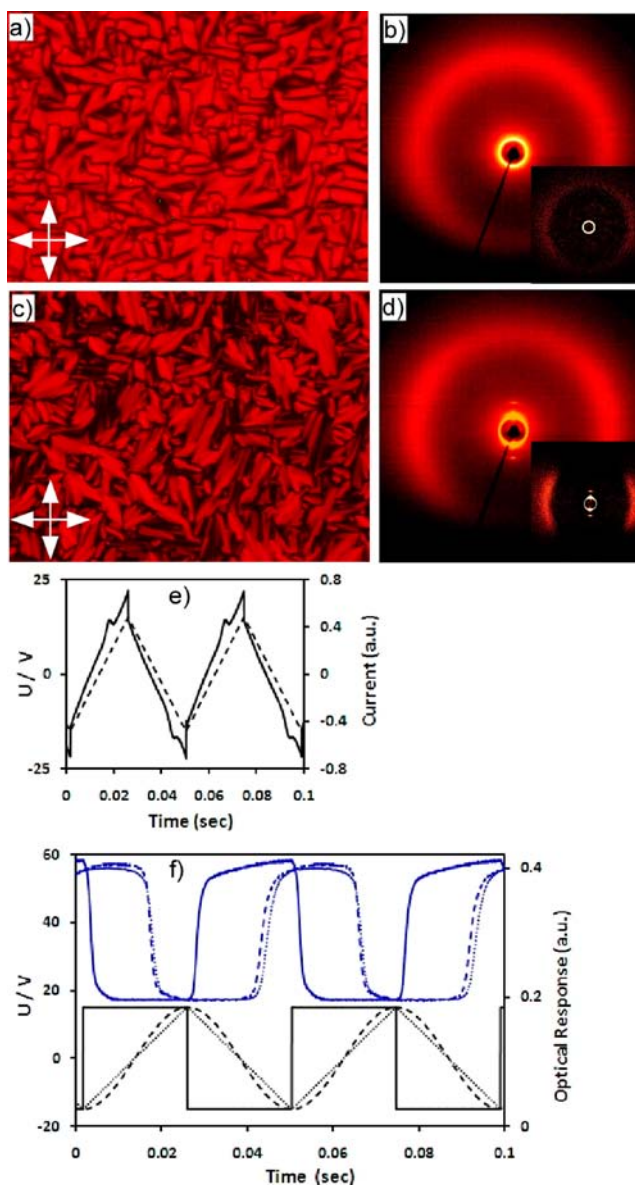


Figure 2. (a–f) Compound 1: (a,c) textures at (a) 141 and (c) 120 °C in a 6 μm ITO-coated cell. (b,d) XRD patterns for a sample on a glass plate at (b) 140 °C [inset: $I = I(140\text{ °C}) - I(160\text{ °C})$] and (d) 120 °C [inset: $I = I(120\text{ °C}) - I(160\text{ °C})$]. (e) Switching current curve (30 V_{pp}, 20 Hz) at 120 °C in a 1.5 μm cell with parallel nylon alignment layers. (f) Optical responses (blue) at 120 °C under different types of waveforms (black, solid line = SW, dashed line = sine waveform, and round-dot dashed line = TW) in the same cell as in (e). Each line style for optical responses corresponds to the same line style for waveforms. Good alignment was achieved in the nylon cell.

time. However, rapidly passing through the temperature range led to the formation of the supercooled glassy state around room temperature, which is in line with the DSC data. The supercooled glassy state was stable once formed, and no crystallization was observed in cells for months.

The XRD patterns confirm the high-T cholesteric phase (Figure 2b) and the low-T SmC* phase (Figure 2d). The inner scattering became gradually more intense and sharper upon cooling a sample from 150 to 135 °C, which is in line with the formation of a cholesteric phase and a subsequent transition to the TGBA* phase at 134 °C. A uniform layer structure was observed to form at 130 °C in agreement with the POM and

EO investigations which indicate a SmC* phase. The XRD patterns did not significantly change upon further cooling to low temperature (Figure S3). First- and second-layer reflections were observed on the meridian of the patterns for this phase, giving a layer spacing of about 3.10 nm and a maximum outer diffuse scattering (ODS) at 0.46 nm, corresponding to the average lateral distances of the molecules (Table S1). The intensity of the ODSs showed four maxima as characteristic for a surface-aligned tilted layer structure. The tilt angle was calculated from the position of these maxima to be in the range of 20–22° (Figure S4), close to the measured optical tilt angle of 21°¹⁹ but much smaller than that (41°) calculated from $\cos \theta = d_C/l_m$ with d_C = SmC* layer spacing and l_m = molecular length (Table S2),²⁰ suggesting strong intercalation between adjacent layers. Generally, the XRD studies with temperature confirmed the phase transitions determined by DSC on heating and cooling, cold crystallization at ~68 °C, and the supercooled glassy state around room temperature (Figures S3 and S5). The XRD pattern of the sample formed by rapidly cooling the isotropic liquid to room temperature (Figure S5) exhibited two peaks which can be interpreted as first- and second-order layer reflections with d values comparable to those of the SmC* phase, indicating that the supercooled glassy state has a similar structure to that of the SmC* phase.

UV–vis Spectra. The UV–vis spectra of five color compounds, including **1** and **2** and their three phenol precursors, are shown in Figure 3. Compounds with an azo

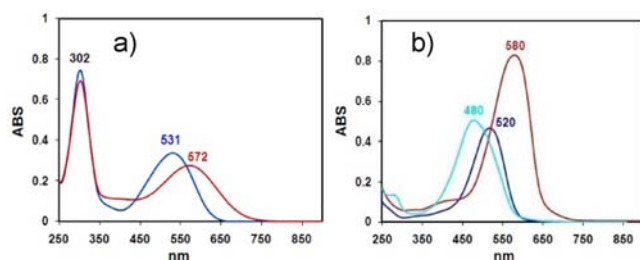


Figure 3. UV–vis spectra of (a) compounds **1** (red) and **2** (blue) and (b) three phenol precursors including the precursors **7** (cyan) and **8** (red) of **1** and the bisphenol precursor¹⁴ (blue) of **2** in dilute CH₂Cl₂ solutions.

linkage (i.e., dimer-like) are deep red in dilute CH₂Cl₂ solutions, while compounds with two azo linkages (i.e., trimer-like) are deep blue in dilute CH₂Cl₂ solutions, indicating that the elongation of conjugated length results in the red-shift of maximum absorption bands. Three phenol precursors exhibit one absorption band with a maximum absorption wavelength of 480, 520, and 580 nm, respectively, and compounds **1** and **2** show two absorption bands with a maximum absorption wavelength of 572 and 531 nm, respectively. The maximum molar extinction coefficient for **1** is 27 700 M⁻¹ cm⁻¹. The absorption bands at the visible region arise from the π – π^* transitions of different chromophore units, and the absorption band at the UV region for **1** and **2** is attributed to the π – π^* transition of the biphenyl unit because their phenol precursors have no such absorption band. The incorporation of a nitro group into compound **7** causes the red-shift of its maximum absorption wavelength by 40 nm. Compared to dimer **2** and its bisphenol precursor,¹⁴ trimers **1** and **8** show the red-shift of their maximum absorption wavelengths by 41 and 60 nm, respectively. This indicates a stronger charge transfer in trimers than in dimers.

SHG Measurements at $\lambda = 1.369 \mu\text{m}$. Since compound **1** is highly absorbing at 532 nm, a Nd:YAG laser ($\lambda = 1.064 \mu\text{m}$) is unsuitable for SHG measurements. Therefore we initially chose a longer wavelength of 1.369 μm where absorption of the second harmonic is lower. This wavelength was obtained by changing the wavelength of the Nd:YAG laser (1.064 μm) via a second-Stokes process by placing a Raman-shifter crystal [Ba(NO₃)₂] after the laser of our usual SHG setup.²¹ Five homeotropically aligned cells with various thicknesses of 1, 2, 3.75, 7, and 11 μm and a gap of 100 μm between in-plane transparent electrodes were utilized. Cell fabrication followed the well-established approach in our lab.¹⁴ Compound **1** was introduced into the cells by capillarity in the isotropic liquid. Upon applying an in-plane E-field ($\sim 5 \text{ V } \mu\text{m}^{-1}$) in the SmC* phase, we achieved very good alignment within the gap region of all cells, indicated by a switching from a uniform dark texture (field off) to a uniform birefringent one (field on). This result supports that we realized the desired homeotropic geometry in which the spontaneous polarization and smectic layers are parallel to the glass plates, and the helicoidal structure with its helical axis perpendicular to the plates is wound or unwound depending on the absence or presence of an in-plane E-field.

The measurements were carried out at normal incidence. Unexpectedly, we observed a strong SHG signal in all the cells both with E-field on and off. The SHG intensity under zero E-field was comparable to or even larger (especially in thicker cells) than that upon applying a strong E-field. These amazing results suggest that we might have realized helicoidal phase matching (HPM) conditions at $\lambda = 1.369 \mu\text{m}$, because wound SmC* structures normally present extremely low SHG responses.

HPM for a SHG process in SmC* helical structures was theoretically predicted decades ago.^{9a,b,22} It is a special condition that permits high conversion efficiencies in the SHG process. When the HPM condition is attained, the light wave vector mismatch is compensated with the wave vector of the helix, similarly to what happens in the so-called quasi PM with periodically poled materials. Few experiments on this subject have been reported up to now. The Takezoe group^{9c} has shown an SHG enhancement from a SmC* phase involving two counter-propagating fundamental waves along the helix. The second harmonic light is generated in both directions of the sample when the second harmonic wavelength is equal to the optical pitch of the helix, i.e., $\lambda = 2pn$, where p is the helical pitch and n an average refractive index. Here we have found that compound **1** exhibits a new type of HPM at $\lambda = 1.369 \mu\text{m}$. This HPM process involves only one fundamental wave propagating in the forward direction. The PM condition is attained for

$$p = \frac{\lambda}{2(n_2 - n_1)} \quad (1)$$

where n_1 and n_2 are refractive indices for the fundamental and second-harmonic waves, respectively. An in-depth explanation of this phenomenon together with the detailed experimental results will be reported in a separate forthcoming paper.²³ Here we will restrict ourselves to outlining how to obtain information about the d_{ij} coefficients in an experiment with the HPM condition.

We observed HPM throughout practically the entire SmC* phase, suggesting that the helical pitch of compound **1** does not vary significantly with temperature. Since the laser spot was much larger than the gap of 100 μm , the conventional method

to determine d_{ij} coefficients by measuring SHG on unwound samples using E-field was unsuitable in this case. Therefore, we measured the SHG intensity of compound **1** in cells with various thicknesses under zero E-field at 120 °C. The polarization of the fundamental light was chosen to be left circular (LC). Under these conditions it can be shown that HPM is achieved, transforming two LC photons into one LC photon (LC + LC → LC), provided that eq 1 is fulfilled. The LC polarization of the SHG signal was explicitly confirmed. The dependence of the SHG intensities on the sample thicknesses is shown in Figure 4a.

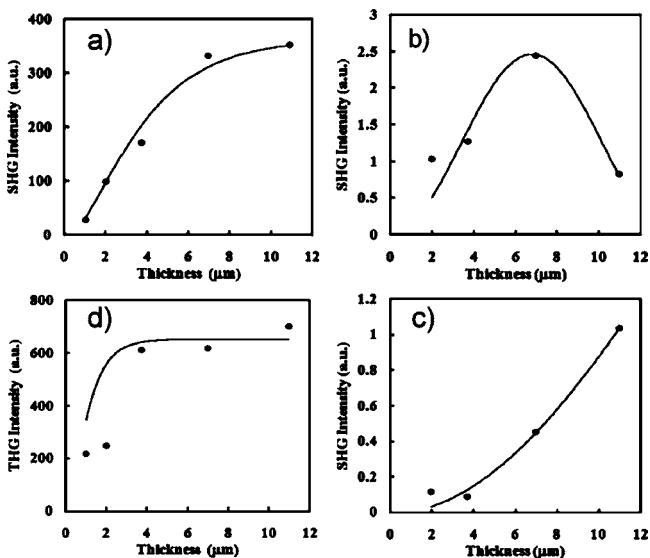


Figure 4. (a–c) SHG and (d) THG signal intensity of compound **1** in cells with various thicknesses of 1, 2, 3.75, 7, and 11 μm . A fit of datapoints to a theoretical curve as (a) expressed by eq 2 for helielectric samples at $\lambda = 1.369 \mu\text{m}$. A fit of datapoints to a theoretical curve as described by eq 3 for (b) unwound samples at p–p configuration at $\lambda = 1.56 \mu\text{m}$ and (c) s–p configuration at $\lambda = 1.56 \mu\text{m}$. A fit of datapoints to a theoretical curve as (d) described by eq 4 in the isotropic liquid at $\lambda = 1.56 \mu\text{m}$.

SHG data analysis is complicated in this case because both the helix and the absorption are involved. Currently there is no theory dealing with the two problems together. To estimate the d_{ij} size, we adopted an expression deduced for the SHG intensity $I_{2\omega}$ generated by a helical structure,²³ which is supposed to be valid at HPM, normal incidence, and neglecting the absorption at the fundamental wavelength:

$$I_{2\omega} = C d_{\text{eff}}^2 I_{\omega}^2 L^2 e^{-\alpha L/2} \frac{\sinh^2(\alpha L/4)}{(\alpha L/4)^2} \quad (2)$$

where C is a constant, L the sample thickness, α the absorption coefficient at 2ω , and d_{eff} an effective nonlinear coefficient depending on the input and output polarizations.

The constant C is deduced by comparing $I_{2\omega}$ with the SHG signal obtained for an $oo \rightarrow o$ conversion of a y -cut quartz crystal, which was used for calibration (here, o stands for ordinary wave, and $d_{11} = 0.4 \text{ pm V}^{-1}$). An absorption coefficient $\alpha = 0.74 \mu\text{m}^{-1}$ was extrapolated from the solution extinction coefficient of **1** at $\lambda = 684.5 \text{ nm}$. The SHG intensity for LC incident light can be fitted well to eq 2 (the continuous line in Figure 4a) with only one fit parameter (the scale factor). From the value of this parameter we obtain $d_{\text{eff}} = 10 \text{ pm V}^{-1}$ for **1**.

Here d_{eff} is the coefficient associated with the LC + LC → LC conversion in the helicoidal SmC^* phase. In general d_{eff} is a complicated linear combination of the four independent non-null d_{ij} elements of the unwound structure.^{9a} However, on the basis of the molecular structure of compound **1**, the d_{22} coefficient in the reference frame of Figure 5a is obviously

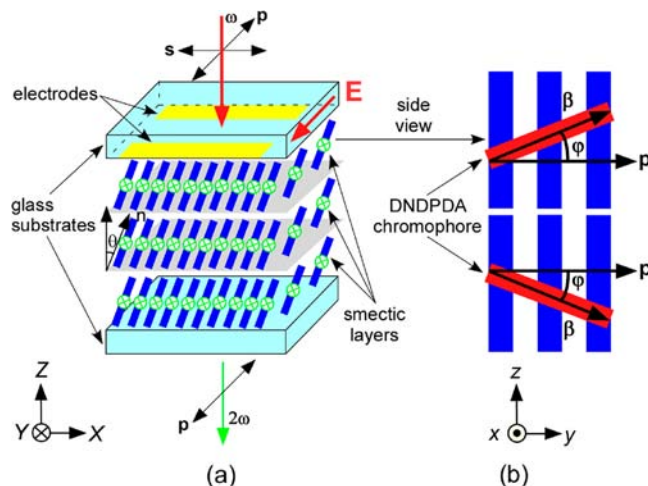


Figure 5. Schemes showing (a) the geometry of FLC molecules of compound **1** with a tilt angle (θ) between the director (n) and the layer normal (i.e., the Z axis) in the aligned zone and polarization of the input and output beams (i.e., p–p and s–p) used in SHG experiments in the XYZ reference frame, and (b) two possible trimer molecular orientations with an angle of φ between the β vector part and the polar p axis (i.e., currently the y axis) in the local molecular xyz reference frame. Note that the dipole in (a) is from positive to negative charges, as used in chemistry. The angle φ has an approximate average of 28° .

dominant over the rest. Hence a much simpler expression for d_{eff} is obtained, $d_{22} = 2\sqrt{2}d_{\text{eff}}^{9a}$ which gives $d_{22} = 28 \text{ pm V}^{-1}$ ($\lambda = 1.369 \mu\text{m}$), a considerably large value for an NLO susceptibility. It is certain that this coefficient is resonance enhanced owing to the material absorption at the second harmonic wavelength.

SHG Measurements at $\lambda = 1.56 \mu\text{m}$. To obtain the d_{ij} coefficients without resonance enhancement, we have also conducted SHG measurements at $\lambda = 1.56 \mu\text{m}$ because the absorption of **1** can be completely neglected at the second harmonic wavelength of 780 nm (Figure 3a). The same type of homeotropically aligned cells as used for SHG at $\lambda = 1.369 \mu\text{m}$ were employed, and we chose four varied thicknesses of 2, 3.75, 7, and 11 μm for SHG measurements. Sample preparation followed the same procedure as above. The measurements were performed at 120 °C at normal incidence. As expected, there was no SHG signal observed with the E-field off but a strong SHG signal within the gap region with the E-field on. This further supports HPM observed at $\lambda = 1.369 \mu\text{m}$. As shown in Figure 5a, the \mathbf{d} tensor is expressed in a reference frame in which Z is perpendicular to the smectic layers and Y is parallel to the polar axis. Input–output light polarization configurations, i.e., input and output parallel or perpendicular to the applied electric field, p or s , were used to measure SHG.

In this configuration the SHG intensity $I_{2\omega}$ is given by

$$I_{2\omega} \propto d_{\text{eff}}^2 I_{\omega}^2 L^2 \frac{\sin^2(\Delta k L/2)}{(\Delta k L/2)^2} \quad (3)$$

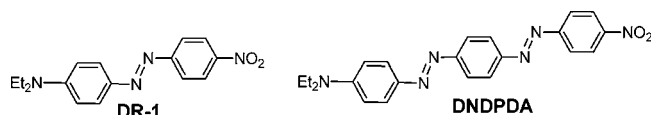
where $d_{\text{eff}} = d_{22}$ for p–p configuration and $d_{\text{eff}} = d_{21}$ for s–p configuration, respectively (see Figure 5a), $\Delta k = 4\pi(n_o(2\omega) - n_e(\omega))/\lambda$ for p–p configuration and $\Delta k = 4\pi(n_o(2\omega) - n_e(\theta, \omega))/\lambda$ for s–p configuration, with $(1/n_e(\theta, \omega))^2 = (\cos\theta/n_e(\omega))^2 + (\sin\theta/n_e(\omega))^2$, are the corresponding refractive index mismatches between the second harmonic and fundamental waves, λ is the wavelength of the fundamental light, and θ is the tilt angle. These data were compared with the SHG signal at the maximum of the first Maker fringe of the quartz crystal under the same conditions of illumination. A fit of SHG intensities of the four samples of **1** at the p–p configuration to the theoretical curve (Figure 4b) as described by eq 3 gives $d_{22} = 6.8 \text{ pm V}^{-1}$ and the dispersion parameter $\Delta n = n_o(2\omega) - n_o(\omega) = 0.058$. A similar fit to the theoretical curve (Figure 4c) for SHG measurements performed at the s–p configuration gives $d_{21} = 1.8 \text{ pm V}^{-1}$ and the corresponding dispersion parameter $\Delta n = n_o(2\omega) - n_e(\theta, \omega) = 0.012$.

It should be noted that the d_{22} coefficient of 28 pm V^{-1} measured at $\lambda = 1.369 \mu\text{m}$ is much larger than that of 6.8 pm V^{-1} measured at $\lambda = 1.56 \mu\text{m}$, strongly supporting that the d_{22} coefficient at $\lambda = 1.369 \mu\text{m}$ is resonance enhanced.

Evaluation of Macroscopic NLO Data at a Microscopic Level. The NLO macroscopic coefficients can be evaluated from molecular and structural parameters. It is well-known that the second-order NLO strength of a bulk organic material originates primarily from the hyperpolarizability (β) of its molecular chromophore. To link macroscopic and microscopic parameters we will use the oriented gas model and assume that the hyperpolarizabilities of compounds **1** and **2** are equal to those of their own chromophores, DNDPDA²⁴ and DR-1.

First of all we discuss the β values of these chromophores. In the case of DR-1 there are published results for the ground-state dipole moment $\mu_g = 7 \text{ D}$ and for $\beta(1.907) = 49 \times 10^{-30} \text{ esu}$ using the Guggenheim and EFISH methods.²⁵ Thus we obtain $\beta\mu_g(1.907) = 343 \times 10^{-48} \text{ esu}$ for DR-1. No EFISH data have been reported for DNDPDA. However, there is one work that gives $\beta\mu_g$ values for both chromophores at several wavelengths calculated from the solvatochromic shifts of the absorption spectra of the chromophores in different solvents.²⁴ As shown in Table 2, the values of DNDPDA are more than twice those of DR-1 at wavelengths between 1.064 and 1.907 μm . It must be noted that the calculated absolute $\beta\mu_g$ value for DR-1 is about 40% larger than its experimental value at 1.907

Table 2. Comparison of $\beta\mu_g$ Values for DR-1 and DNDPDA Chromophores at a Variety of Wavelengths^a



	$\beta\mu_g (\times 10^{-48} \text{ esu})$				
	1.064 μm	1.30 μm	1.56 μm	1.70 μm	1.907 μm
DR-1	1964	839	600	542	488
DNDPDA	7924	2063	1353	1198	1058
ratio	4.03	2.46	2.26	2.21	2.17

^aThe $\beta\mu_g$ values are calculated using eq S1 for chromophores with donor–acceptor charge transfer (see the detailed calculation and Table S3 in Supporting Information). The values of some parameters used for the calculation are from the literature²⁴ in which the $\beta\mu_g$ values for DNDPDA at all wavelengths were incorrectly shown. The corrected values are shown in this table.

μm obtained by EFISH (i.e., 488 vs 343).²⁵ The discrepancy is due to the fact that the solvatochromic method²⁶ is a rather indirect technique to obtain $\beta\mu_g$. Therefore we will adopt the reported EFISH data for DR-1²⁵ and also consider that the relative ratios between $\beta\mu_g$ of DNDPDA and DR-1 in Table 2 are correct, based on their mutual conjugation lengths.

Using the two-level model,²⁷ we calculate $\beta(1.56) = 65 \times 10^{-30} \text{ esu}$ ($\lambda_{\text{max}} = 531 \text{ nm}$) for compound **2** from the experimental value at 1.907 μm .²⁵ According to the $\beta\mu_g$ ratios in Table 2 we obtain $\beta(1.56) = 147 \times 10^{-30} \text{ esu}$ ²⁸ for compound **1**, assuming that both DNDPDA and DR-1 chromophores have a similar μ_g value.

Next we turn to discuss some structural aspects of the molecules in the mesophase. In compound **1**, the DNDPDA chromophore adopts a configuration with an angle $\varphi = 28^\circ$ with respect to the FLC's polar axis. This means that the β vector component also makes the same angle φ with the polar axis (Figure 5b). On the other hand, it is known that an FLC has a two-fold rotation axis along its polar axis due to head–tail symmetry. Hence we assume that the smectic layers in **1** consist of a 50:50 mixture of two possible molecular orientations of **1** (Figure 5b).

For our model to be more realistic, we permit some disorder of the molecules in the material, with the possibility of molecular rotation around the z axis (see Figure 5b). In an elementary approach, the disorder is simply characterized by a deviation of the molecular plane from its average position, with an angle Ψ between the y and Y axes (see Figure 5). The term $\langle \cos\Psi \rangle$ represents the degree of polar order of the material and links the spontaneous polarization P_s with the FLC's molecular dipole moment μ_p along the polar axis through the expression $P_s = N\mu_p \langle \cos\Psi \rangle$, where N is the number density of molecules. If the density of **1** is assumed to be $\rho = 1 \text{ g cm}^{-3}$, then $N = 3.27 \times 10^{26} \text{ m}^{-3}$. Taking $\mu_p = 1.0 \text{ D}$ along the polar axis (calculated using the AM1 model) and the experimental P_s at 120 °C we get $\langle \cos\Psi \rangle = 0.23$, quite similar to compound **2**.

Finally we follow exactly the same approach used in a previous work for compound **2** to compute the four independent d_{ij} coefficients²⁹ (see the detailed equations in Supporting Information). The local-field factors that also appear in the expressions for d_{ij} are assumed to be the same for both **1** and **2**. After careful numerical calculations we obtain the following coefficients: $d_{22} = 6.02$, $d_{21} = 2.56$, $d_{23} = 2.45$, and $d_{14} = 0.05 \text{ pm V}^{-1}$. Given the crudeness of this model and the amount of approximations, the agreement with the experimental results, $d_{22} = 6.8$, $d_{21} = 1.8 \text{ pm V}^{-1}$, is rather remarkable.

THG Measurements at $\lambda = 1.56 \mu\text{m}$. Besides a strong SHG response in the SmC* phase, compound **1** was also found to exhibit a strong THG response. Contrary to SHG, THG occurs in centrosymmetric media. The effect is driven by the third-order susceptibility tensor $\chi^{(3)}$. To characterize the THG of the material, measurements were carried out in the isotropic liquid (150 °C) only for simplicity. In the isotropic state the effect is determined by a single coefficient $\chi^{(3)}$. We used a laser beam with a fundamental wavelength of 1.56 μm to perform THG measurements at normal incidence. To determine $\chi^{(3)}$, five cells with thicknesses of 1, 2, 3.75, 7, and 11 μm were utilized. A BK7 glass plate with a thickness of 150 μm , a susceptibility of $\chi_{\text{BK7}}^{(3)} = 4.7 \times 10^{-14} \text{ esu}$, and a coherence length of $l_c = \pi/\Delta k(\text{BK7}) = 16.4 \mu\text{m}$ was adopted as a reference. Note that BK7 is completely transparent at the third harmonic wavelength of 520 nm. As expected, the THG light always had the same polarization as the fundamental light. Compound **1** is

highly absorbing at $\lambda = 520$ nm and transparent for the fundamental wave, therefore the THG intensity is given by the expression (see details in Supporting Information):

$$I_{3\omega} \propto \frac{|\chi^{(3)}|^2}{n_{3\omega}^3 n_{\omega}^3} I_{\omega}^3 L^2 e^{-\alpha L/2} \frac{\sin^2(\Delta k L/2) + \sinh^2(\alpha L/4)}{(\Delta k L/2)^2 + (\alpha L/4)^2} \quad (4)$$

where $\Delta k = 6\pi(n_{3\omega} - n_{\omega})/\lambda$ and α is the absorption coefficient at 3ω . For neat compound **1**, $\alpha = 2.57 \mu\text{m}^{-1}$ was extrapolated from its solution extinction coefficient at $\lambda = 520$ nm.

The THG intensities vs sample thicknesses are depicted in Figure 4d. By fitting this curve to eq 4 some information about $\chi^{(3)}$ can be obtained. In this case, due to the strong absorption at the third harmonic wavelength, Δk and $\chi^{(3)}$ cannot be obtained separately, but only a combination of both is experimentally accessible (see the detailed data process in Supporting Information). The lower limit for $\chi^{(3)}$ is 1.5×10^{-11} esu, and taking a conservative value for $n_{3\omega} - n_{\omega} = 0.18$ we estimate $\chi^{(3)} = \sim 3 \times 10^{-11}$ esu (i.e., $\sim 4.2 \times 10^{-19} \text{ m}^2 \text{ V}^{-2}$).³⁰ This value is comparable to the largest value (4.8×10^{-11} esu at $\lambda = 1.5 \mu\text{m}$) measured for a PMMA polymer attached with a DNDPDA dye pendant (44 wt% dye content),³¹ further verifying our THG measurements for compound **1** with a DNDPDA dye density of ~ 22 wt%. As far as we know, compound **1** exhibits the largest third-order susceptibility to date for liquid crystals,³² and its $\chi^{(3)}$ value is much larger than $\chi^{(3)} = 0.74 \times 10^{-11}$ esu at $\lambda = 1.9 \mu\text{m}$ for 4-diethylamino-4'-nitrostilbene (DEANS) in single crystals³³ and the largest $\chi^{(3)}$ value of 0.58×10^{-11} esu at $\lambda = 1.064 \mu\text{m}$ (0.056×10^{-11} esu at $\lambda = 1.579 \mu\text{m}$) for a series of nematic liquid crystalline polymers.³⁴ However, the obtained result is resonance enhanced. A characterization of the THG in a transparent regime is out of our present experimental facilities.

SUMMARY AND CONCLUSIONS

We report a laterally azo-bridged mesogen **1** which incorporates a strong chromophore along its polar axis. It is remarkable that compound **1**, which links three rod-like units together via two azo groups to form such a huge molecule, exhibits a ground-state enantiotropic SmC* (i.e., ferroelectric) phase with a broad phase temperature range of 103 K during cooling. It is worthy to note that, like rod-shaped liquid crystals for display applications, trimer **1** can readily achieve good planar alignment in cells with parallelly buffed organic (e.g., nylon) alignment layers. In such a surface stabilized cell with a bookshelf geometry, this compound shows a bistable ferroelectric switching instead of an analogue V-shaped switching. Good homeotropic alignment was also achieved upon applying a relatively weak in-plane E-field.

Compound **1** exhibits a previously unreported HPM process at $\lambda = 1.369 \mu\text{m}$. By SHG measurements we obtained the d_{22} coefficient of 28 pm V^{-1} , the largest NLO coefficient reported to date for FLCs including bent-core NLO materials³⁵ (Table 3). This value is comparable to the NLO coefficient of $d_{33} = 27 \text{ pm V}^{-1}$ for widely used commercial periodically poled lithium niobate (PPLN) crystals and clearly enables viable applications of FLCs in nonlinear optics. The lasers we adopted for SHG studies span the full wavelength range of 1.3–1.55 μm in telecommunication applications. Besides strong SHG strength, compound **1** also exhibits a strong THG response with a $\chi^{(3)}$ value of $\sim 3 \times 10^{-11}$ esu at $\lambda = 1.56 \mu\text{m}$. To the best of our knowledge, this is the largest third-order susceptibility (measured using a THG technique) reported to date for liquid

Table 3. Comparison of Nonlinear Coefficients (d_{ij}) Measured at the Fundamental Wavelength (λ) and Maximum Absorption Wavelengths (λ_{max}) for Milestone FLC Materials^a

FLC materials	λ_{max} nm	d_{ij} pm V ⁻¹ ($\lambda/\mu\text{m}$)
DOBAMBC	no data	$d_{\text{eff}} = 0.0011$ (1.064) ^{12l}
W314	270	$d_{22} = 0.63$ (1.064) ^{12b}
Roche1	380	$d_{22} = 5.0$ (1.064) ^{12f}
2 (dimer)	531	$d_{22} = 17$ (1.064), ¹⁴ 4.5 (1.6) ²⁹
P-9-O-PIMB	340	$d_{22} = 3.8$ (1.064) ^{35a}
Ros1 ^b	485	$d_{22} = 48$ (1.064), 8 (1.6) ^{35f}
1 (trimer)	572	$d_{22} = 28$ (1.369), 6.8 (1.56)

^aIn most cases only d_{22} is shown because this is the coefficient that is optimized from the viewpoint of chemical design. All materials possess a SmC* phase except for P-9-O-PIMB and Ros 1, two milestone bent-core mesogens. Although two analogues in the P-*n*-O-PIMB family were reported to show larger d_{22} coefficients by different groups,^{35b,c} we choose to show a smaller value for P-9-O-PIMB for a purpose of better comparison because it was measured by the same group in which compounds **1**, **2**, and Ros1 were measured under the same SHG setup. ^bRos1 has an apolar columnar (Col) phase that is unsuitable for SHG applications, and its d_{22} coefficient was extrapolated from a 50% mixture which has a ground-state antiferroelectric (SmC_aP_A) phase and a field-induced ferroelectric (SmC_sP_F) phase. Therefore, the practical d_{22} values for Ros1 should be half of those listed in this table (i.e., $d_{22} = 24$ (1.064 μm), 4 (1.6 μm) pm V⁻¹).^{35f}

crystals. This work highlights that a combination of ferroelectricity and large macroscopic nonlinearities via elaborate molecular design and tailoring can lead to interesting functional FLC materials with potentially useful NLO and EO properties.

ASSOCIATED CONTENT

Supporting Information

Synthetic procedures for **1** and **5–8**, experimental procedures, relationships between β and d_{ij} , detailed THG data process for **1**, Figures S1–S5, and Tables S1–S3. The material is available free of charge via the Internet at <http://pubs.acs.org>.

AUTHOR INFORMATION

Corresponding Author

zhangyongqiang731@yahoo.com; j.etxeba@ehu.es

Notes

The authors declare no competing financial interest.

ACKNOWLEDGMENTS

This work was supported by NSF (U.S.A.) grants (OII-0539835 and IIP-0646460) to Displaytech Inc. (acquired by Micron Technology Inc.), the MEC-FEDER of Spain-EU (project MAT2009-14636-C03-03), and by the Basque Government (project GI/IT-449-10). Technical and human support provided by the Laser Facility of the SGIker (UPV/EHU, MICINN, GV/EJ, ESF) is gratefully acknowledged.

REFERENCES

- (1) (a) Shi, Y.; Zhang, C.; Zhang, H.; Bechtel, J. H.; Dalton, L. R.; Robinson, B. H.; Steier, W. H. *Science* **2000**, 288, 119. (b) Lee, M.; Katz, H. E.; Erben, C.; Gill, D. M.; Gopalan, P.; Heber, J. D.; McGee, D. J. *Science* **2002**, 298, 1401. (c) Hales, J. M.; Matichak, J.; Barlow, S.; Ohira, S.; Yesudas, K.; Bredas, J.-L.; Perry, J. W.; Marder, S. R. *Science* **2010**, 327, 1485–1488.

- (2) (a) *Nonlinear optics of organic molecules and polymers*; Nalwa, H. S., Miyata, S., Eds.; CRC Press, Inc: Boca Raton, FL, 1996. (b) Yitzchaik, S.; Marks, T. J. *Acc. Chem. Res.* **1996**, *29*, 197–202. (c) Marder, S. R. *Chem. Commun.* **2006**, 131. (d) Innocenzi, P.; Lebeau, B. *J. Mater. Chem.* **2005**, *15*, 3821. (e) Coe, B. J. *Acc. Chem. Res.* **2006**, *39*, 383. (f) Sullivan, P. A.; Dalton, L. R. *Acc. Chem. Res.* **2010**, *43*, 10–18.
- (3) Dalton, L. R.; Sullivan, P. A.; Bale, D. H. *Chem. Rev.* **2010**, *110*, 25–55.
- (4) Lagerwall, S. T. *Ferroelectric and antiferroelectric liquid crystals*; Wiley-VCH: Weinheim, Germany, 1999.
- (5) Zhang, Y.; Etxebarria, J. Ferroelectric liquid crystals for nonlinear optical applications. In *Liquid crystals beyond displays*; Li, Quan, Ed.; Wiley: Hoboken, NJ, 2012, 111–156.
- (6) Champagne, B.; Guthmuller, J.; Perreault, F.; Soldera, A. *J. Phys. Chem. C* **2012**, *116*, 7552–7560.
- (7) Etxebarria, J.; Ros, M. B. *J. Mater. Chem.* **2008**, *18*, 2919–2926.
- (8) (a) Lee, S. K.; Heo, S.; Lee, J. G.; Kang, K.-T.; Kumazawa, K.; Nishida, K.; Shimbo, Y.; Takanishi, Y.; Watanabe, J.; Doi, T.; Takahashi, T.; Takezoe, H. *J. Am. Chem. Soc.* **2005**, *127*, 11085–11091. (b) Hennrich, G.; Omenat, A.; Asselberghs, I.; Foerier, S.; Clays, K.; Verbiest, T.; Serrano, J. L. *Angew. Chem., Int. Ed.* **2006**, *45*, 4203–4206. (c) Gorecka, E.; Pocięcha, D.; Matraszek, J.; Mieczkowski, J.; Shimbo, Y.; Takanishi, Y.; Takezoe, H. *Phys. Rev. E* **2006**, *73*, 031704. (d) Okada, Y.; Matsumoto, S.; Takanishi, Y.; Ishikawa, K.; Nakahara, S.; Kishikawa, K.; Takezoe, H. *Phys. Rev. E* **2005**, *72*, 020701(R). (e) Miyajima, D.; Araoka, F.; Takezoe, H.; Kim, J.; Kato, K.; Takata, M.; Aida, T. *Science* **2012**, *336*, 209. (f) Hough, L. E.; Jung, H. T.; Krüerke, D.; Heberling, M. S.; Nakata, M.; Jones, C. D.; Chen, D.; Link, D. R.; Zasadzinski, J.; Heppke, G.; Rabe, J. P.; Stocker, W.; Körblová, E.; Walba, D. M.; Glaser, M. A.; Clark, N. A. *Science* **2009**, *325*, 456–460. (g) Koike, M.; Yen, C.-C.; Liu, Y.; Tsuchiya, H.; Tokita, M.; Kawachi, S.; Takezoe, H.; Watanabe, J. *Macromolecules* **2007**, *40*, 2524–2531.
- (9) (a) Drevensk-Olenik, I.; Copic, M. *Phys. Rev. E* **1997**, *56*, 581–591. (b) Hoshi, H.; Chung, D. H.; Ishikawa, K.; Takezoe, H. *Phys. Rev. E* **2001**, *63*, 056610. (c) Yoo, J. G.; Choi, S. W.; Hoshi, H.; Ishikawa, K.; Takezoe, H.; Schadt, M. *Jpn. J. Appl. Phys.* **1997**, *36*, L1168–L1171.
- (10) Cai, W.; Vasudev, A. P.; Brongersma, M. L. *Science* **2011**, *333*, 1720–1723.
- (11) (a) Verbiest, T.; Houbrechts, S.; Kauranen, M.; Clays, K.; Persoons, A. *J. Mater. Chem.* **1997**, *7*, 2175–2189. (b) Dalton, L. R.; Steier, W. H.; Robinson, B. H.; Zhang, C.; Ren, A.; Garner, S.; Chen, A.; Londergan, T.; Irwin, L.; Carlson, B.; Fifield, L.; Phelan, G.; Kincaid, C.; Amend, J.; Jen, A. *J. Mater. Chem.* **1999**, *9*, 1905–1920.
- (12) (a) Shtykov, N. M.; Barnik, M. I.; Beresnev, L. A.; Blinov, L. M. *Mol. Cryst. Liq. Cryst.* **1985**, *124*, 379–390. (b) Walba, D. M.; Ros, M. B.; Clark, N. A.; Shao, R.; Robinson, M. G.; Liu, J. Y.; Johnson, K. M.; Doroski, D. J. *J. Am. Chem. Soc.* **1991**, *113*, 5471–5474. (c) Yoshino, K.; Utsumi, M.; Morita, Y.; Sadohara, Y.; Ozaki, M. *Liq. Cryst.* **1993**, *14*, 1021–1032. (d) Trollsås, M.; Orrenius, C.; Sahlén, F.; Gedde, U. W.; Norin, T.; Hult, A.; Hermann, D.; Rudquist, P.; Komitov, L.; Lagerwall, S. T.; Lindström, J. *J. Am. Chem. Soc.* **1996**, *118*, 8542–8548. (e) Artal, C.; Ros, M. B.; Serrano, J. L.; Pereda, N.; Etxebarria, J.; Folcia, C. L.; Ortega, J. *Macromolecules* **2001**, *34*, 4244–4255. (f) Schmitt, K.; Herr, R.-P.; Schadt, M.; Fünfschilling, J.; Buchecker, R.; Chen, X. H.; Benecke, C. *Liq. Cryst.* **1993**, *14*, 1735–1752. (g) Keller, P.; Shao, R.; Walba, D. M.; Brunet, M. *Liq. Cryst.* **1995**, *18*, 915–918. (h) Walba, D. M.; Keller, P.; Shao, R.; Clark, N. A.; Hillmyer, M.; Grubbs, R. H. *J. Am. Chem. Soc.* **1996**, *118*, 2740–2741. (i) Fazio, V. S. U.; Lagerwall, S. T.; Zauls, V.; Schrader, S.; Busson, P.; Hult, A.; Motschmann, H. *Eur. Phys. J. E: Soft Matter Biol. Phys.* **2000**, *3*, 245–251. (j) Trollsås, M.; Sahlén, F.; Gedde, U. W.; Hult, A.; Hermann, D.; Rudquist, P.; Komitov, L.; Lagerwall, S. T.; Stebler, B.; Lindström, J.; Rydlund, O. *Macromolecules* **1996**, *29*, 2590–2598. (k) Espinet, P.; Etxebarria, J.; Folcia, C. L.; Ortega, J.; Ros, M. B.; Serrano, J. L. *Adv. Mater.* **1996**, *8*, 745–748. (l) Ozaki, M.; Utsumi, M.; Gotou, T.; Morit, Y.; Daido, K.; Sadohara, Y.; Yoshino, K. *Ferroelectrics* **1991**, *121*, 259–274.
- (13) (a) Walba, D. M.; Dyer, D. J.; Sierra, T.; Cobben, P. L.; Shao, R.; Clark, N. A. *J. Am. Chem. Soc.* **1996**, *118*, 1211. (b) Walba, D. M.; Xiao, L.; Keller, P.; Shao, R.; Link, D.; Clark, N. A. *Pure Appl. Chem.* **1999**, *71*, 2117. (c) Walba, D. M.; Xiao, L.; Korblova, E.; Keller, P.; Shoemaker, R.; Nakata, M.; Shao, R.; Link, D. R.; Coleman, D. A.; Clark, N. A. *Ferroelectrics* **2004**, *309*, 77.
- (14) Zhang, Y.; Martinez-Perdiguero, J.; Baumeister, U.; Walker, C.; Etxebarria, J.; Prehm, M.; Ortega, J.; Tschierske, C.; O’Callaghan, M. J.; Harant, A.; Handschy, M. *J. Am. Chem. Soc.* **2009**, *131*, 18386–18392.
- (15) Abdel-Magid, A. F.; Carson, K. G.; Harris, B. D.; Maryanoff, C. A.; Shah, R. D. *J. Org. Chem.* **1996**, *61*, 3849.
- (16) Haghbeen, K.; Tan, E. W. *J. Org. Chem.* **1998**, *63*, 4503. Note that 14 g of K_2CO_3 should be used instead of 1.4 g mentioned in the experimental procedure of this reference.
- (17) (a) Dierking, I.; F. Gießelmann, F.; Zugenmaier, P. *Liq. Cryst.* **1994**, *17*, 17–22. (b) Dierking, I. *Liq. Cryst.* **1999**, *26*, 83–95. (c) Kašpar, M.; Novotná, V.; Glogarová, M.; Hamplová, V.; Pocięch, D. *Liq. Cryst.* **2010**, *37*, 129–137.
- (18) The spontaneous polarization was measured in a 4.3 μm cell with parallel polyimide (PI) alignment layers using an SW E-field ($\pm 30\text{V}$, 5 Hz).
- (19) The optical tilt angle was measured in a 1.5 μm cell with parallel nylon alignment layers at 120 °C using an SW E-field ($\pm 15\text{V}$, 20 Hz).
- (20) The molecular length l_m is the sum (4.1 nm) of the molecular length (3.86 nm) with a fully stretched chain (Chem3D) and van der Waals diameter (0.24 nm) of H atom.
- (21) Pereda, N.; Folcia, C. L.; Etxebarria, J.; Ortega, J.; Ros, M. B. *Liq. Cryst.* **1998**, *24*, 451.
- (22) Belyakov, V. A.; Shipov, N. V. *Phys. Lett.* **1981**, *86A*, 94–97.
- (23) Etxebarria, J.; Ortega, J.; Folcia, C. L.; Zhang, Y.; Walker, C. *Phys. Rev. E* submitted.
- (24) The full name of the chromophore is *N,N*-diethyl-4-((*E*)-(4-((*E*)-(4-nitrophenyl)diazanyl)phenyl)diazanyl)aniline. It can be readily synthesized by following an approach to an analogue in the following reference. Amano, M.; Kaino, T. *J. Appl. Phys.* **1990**, *68*, 6024.
- (25) Cheng, L. T.; Tam, W.; Stevenson, S. H.; Meredith, G. R.; Rikken, G.; Marder, S. R. *J. Phys. Chem.* **1991**, *95*, 10631–10643.
- (26) Suzuki, H.; Hiratsuka, H. *Proc. SPIE* **1988**, *971*, 97.
- (27) Spackman, M. A. *J. Phys. Chem.* **1989**, *93*, 7594.
- (28) The calculated value of $\beta(1.56)$ using the MOPAC molecular modeling is equal to 103×10^{-48} esu at $\lambda = 1.56 \mu\text{m}$, smaller than this value.
- (29) Martinez-Perdiguero, J.; Zhang, Y.; Walker, C.; Etxebarria, J.; Folcia, C. L.; Ortega, J.; O’Callaghan, M. J.; Baumeister, U. *J. Mater. Chem.* **2010**, *20*, 4905–4909.
- (30) The conversion factor between esu and MKS unit is: $\chi^{(3)}$ (esu) = $(9 \times 10^8/4\pi) \chi^{(3)}$ ($\text{m}^2 \text{V}^{-2}$).
- (31) Kaino, T.; Tomaru, S.; Kurihara, T.; Amano, M. *Mater. Res. Soc. Symp. Proc.* **1992**, *247*, 179–190.
- (32) Only the third-order susceptibilities measured using THG for liquid crystals are used for comparison because the $\chi^{(3)}$ value for the same material in other third-order processes, such as degenerate four-wave mixing (DFWM) could be several orders of magnitude larger than $\chi^{(3)}$ from THG. Nalwa, H. S. *Adv. Mater.* **1993**, *5*, 341–358.
- (33) Kurihara, T.; Kabayashi, H.; Kubodera, K.; Kaino, T. *Opt. Commun.* **1991**, *84*, 149–154.
- (34) Smith, D. A.; Coles, H. J. *Liq. Cryst.* **1993**, *14*, 937.
- (35) (a) Ortega, J.; Gallastegui, J. A.; Folcia, C. L.; Etxebarria, J.; Gimeno, N.; Ros, M. B. *Liq. Cryst.* **2004**, *31*, 579–584. (b) Macdonald, R.; Kentischer, F.; Warnick, P.; Heppke, G. *Phys. Rev. Lett.* **1998**, *81*, 4408–4411. (c) Araoka, F.; Thisayukta, J.; Ishikawa, K.; Watanabe, J.; Takezoe, H. *Phys. Rev. E* **2002**, *66*, 021705. (d) Folcia, C. L.; Alonso, I.; Ortega, J.; Etxebarria, J.; Pintre, I.; Ros, M. B. *Chem. Mater.* **2006**, *18*, 4617. (e) Pintre, I. C.; Gimeno, N.; Serrano, J. L.; Ros, M. B.; Alonso, I.; Folcia, C. L.; Ortega, J.; Etxebarria, J. *J. Mater. Chem.* **2007**, *17*, 2219–2227. (f) Pintre, I. C.; Serrano, J. L.; Ros, M. B.; Martinez-Perdiguero, J.; Alonso, I.; Ortega, J.; Folcia, C. L.; Etxebarria, J.

Alicante, R.; Villacampa, B. *J. Mater. Chem.* **2010**, *20*, 2965–2971 .
Note that important discrepancies were found for the d coefficients of the P- n -O-PIMB family reported by different groups, and the reasons for the disparities are still unclear.